

# BBNet: accurate neural network emulator for primordial light element abundances

Fan Zhang,<sup>1,2</sup> Hang Diao,<sup>1</sup> Bohua Li,<sup>3,\*</sup> Joel Meyers,<sup>4</sup> and Paul R. Shapiro<sup>5</sup>

<sup>1</sup>*State Key Laboratory of Ocean Sensing & Ocean College,  
Zhejiang University, Zhoushan, Zhejiang 316000, China*

<sup>2</sup>*Kavli Institute for Astrophysics and Space Research,  
Massachusetts Institute of Technology, Cambridge, MA, 02139, USA*

<sup>3</sup>*Guangxi Key Laboratory for Relativistic Astrophysics, School of Physical Science and Technology,  
Guangxi University, Nanning, Guangxi, 530004, China*

<sup>4</sup>*Department of Physics, Southern Methodist University, Dallas, TX 75275, USA*

<sup>5</sup>*Department of Astronomy, The University of Texas at Austin, Austin, TX 78712, USA*

Big-Bang Nucleosynthesis (BBN) predictions of primordial light-element abundances offer a powerful probe of early-Universe physics. However, high-accuracy numerical BBN calculations have become a major computational bottleneck for large-scale cosmological inferences due to the complex nuclear network. Here we present **BBNet**, a fast and accurate deep learning emulator for primordial abundances. The training data are generated by full numerical calculations using two public BBN codes, **PARthENoPE** and **AlterBBN**, modified to accommodate extended cosmologies that include dark radiation and a stiff equation of state. The network employs a residual multi-head architecture to capture convoluted physical relationships. **BBNet** produces primordial helium-4 and deuterium abundances with negligible errors in milliseconds per sample, achieving a speed-up of up to  $10^4$  times relative to first-principles solvers while remaining unbiased over wide parameter ranges. Therefore, our emulator can supersede traditional simplified numerical prescriptions that compromise accuracy for speed. Based on extensive assessments of its performance, we conclude that **BBNet** is an optimal solution to the theoretical prediction of primordial element abundances. It will serve as a reliable tool for precision cosmology and new-physics searches.

## I. INTRODUCTION

Primordial abundances of the light elements produced during big-bang nucleosynthesis (BBN) present a direct probe of the physical conditions in the early Universe [1–3]. The agreement between their predictions and observations supports the concordance hot big-bang cosmology [4–6]. In particular, the primordial helium and deuterium abundances together offer one of the most stringent constraints on the standard  $\Lambda$ CDM model (e.g., on the baryon density) as well as new physics beyond the Standard Model (BSM) [7–10].

The precision of the BBN constraints depends on accurate theoretical calculations of the BBN reaction network [11–13]. However, the nuclear reaction rates that enter the BBN network are subject to laboratory measurement uncertainties [14–17], and the propagated uncertainties on the primordial element abundances from BBN calculations are often significant [18–21]. In the case of the D/H abundance, the theoretical uncertainty is in fact the dominant source of error compared with the uncertainty from astrophysical measurements [22–24]. Additional uncertainties may arise from the prescription of neutrino physics during weak decoupling, which partially overlaps the early stage of BBN [25, 26]. Therefore, it is crucial that the BBN calculation itself, which involves solving the set of coupled ordinary differential equations (ODEs) that describe the BBN network, does not add to the theoretical errors.

Modern numerical solvers have been developed to meet this need, including public BBN codes **PARthENoPE** [27–29], **AlterBBN** [30, 31], **PRIMAT** [32], **PRyMordial** [33], **pyBBN** [34], etc. Most of these methods are updates of the earlier Kawano code, **NUC123** [35], which is itself based on the historical Wagoner code [36, 37]. They yield accurate solutions of primordial abundances, while some of the codes entertain various BSM scenarios. However, the computational demands of these first-principles methods are high; even the fastest BBN codes should take  $\mathcal{O}(0.1)$  seconds for a single execution in simplified settings and longer in full settings. Taking **PARthENoPE** for example, a single run can cost tens of seconds on a CPU with its complete 26-nuclide configuration. Such costs pose a serious challenge to parameter inference tasks based on standard techniques such as Markov chain Monte Carlo (MCMC) sampling, which typically require thousands of evaluations to explore posterior distributions. The burden is exacerbated in BSM scenarios that involve additional parameters, e.g., variations of fundamental constants, dark radiation, nonzero neutrino chemical potentials, sterile neutrinos, [29, 31, 33, 34, 38, 39], etc.

This computational bottleneck often forces compromises in the numerical treatments of BBN calculations. Some methods adopt or provide simplified nuclear reaction networks, achieving faster computation at the cost of introducing systematic biases. For example, even the recently developed codes **PRyMordial** and **LINX** consider only 62 reactions in their “full” network with 12 nuclides [40], in contrast to the “complete” network of 100 reactions in **PARthENoPE** and **AlterBBN**. Another approach to speed up is to use less accurate integration algorithms for

\* bohuali@gxu.edu.cn

the ODEs. **AlterBBN** offers a spectrum of ODE solvers to explore the speed-accuracy trade-off [31]. Apart from these efforts, the interface between the BBN code and Bayesian inference applications are optimized in the **LINX** package, which enables gradient-assisted inference that achieves faster convergence than MCMC [40].

In this paper, we introduce **BBNet**, a deep learning emulator for efficient and accurate BBN computations of primordial element abundances. We employ multi-layer perceptrons with residual connections as the main architecture of **BBNet**, together with a multi-head attention module [41–43]. Based on the training data generated by existing BBN codes, **ParthENoPE** and **AlterBBN**, our emulator can output the primordial helium and deuterium abundances in  $\sim 6$  ms per sample on an NVIDIA A100 GPU and in  $\sim 2.5$  ms per sample with batch processing. This corresponds to a speed-up of  $\mathcal{O}(10^4)$  times compared with first-principles BBN calculations.

The high computational efficiency of **BBNet** is particularly helpful in exploring scenarios that involve BSM physics. In its current version, we consider an extra dark radiation component, parameterized by the number of extra relativistic species, and a possible kination/stiff phase in the early Universe [44]. The latter is a pre-BBN era in the expansion history during which the total energy density of the Universe is dominated by the kinetic energy of a scalar field [45–48]. During kination or a stiff phase, the equation of state (EoS) of the Universe is given by that of a stiff fluid,  $\bar{w} \equiv P/\bar{\rho} = 1$ . It can occur in extended cosmological models with quintessence, ultralight scalar field dark matter, QCD axion [49–52], etc.

**BBNet** attains exceptional emulation accuracy in addition to its speed advantage. The relative root mean square (RMS) errors between the predicted primordial abundances,  $Y_{\text{P}}$  and D/H, and their ground-truth values from the BBN calculations are typically of the order of 0.1% or less. The predictions of the emulator are also unbiased, achieving a mean percentage error below 0.1%. The errors from **BBNet** emulations are thus negligible compared with current theoretical and observational uncertainties of  $Y_{\text{P}}$  and D/H. The unprecedented speed and accuracy of **BBNet** present a solution to the BBN computational bottleneck, reducing the cost of high-dimensional cosmological analyses by orders of magnitude. By integrating **BBNet** into MCMC pipelines, one can perform efficient joint analyses of large cosmological data sets based on extended models without compromising the accuracy of BBN computations.

The remainder of this paper is organized as follows. Sec. II presents a brief overview of BBN physics and then describes the BBN codes and the cosmological model considered in this work. Sec. III provides a detailed description of our data generation strategy and the architecture of the **BBNet** neural network emulator. Sec. IV discusses the optimization protocols, regularization techniques, and validation procedures for training the emulator. In Sec. V, we present comprehensive performance benchmarks and accuracy assessments. Sec. VI com-

pare the performance of **BBNet** with those of existing fast approximation modes internal to **ParthENoPE** and **AlterBBN**. Finally, Sec. VII summarizes our key conclusions and proposes directions for future research.

## II. BBN CALCULATION AND COSMOLOGICAL MODEL

This section reviews the key aspects of BBN, including the thermal history of the early Universe, the nuclear reaction network, and the numerical techniques required by BBN calculations. We then describe the BSM physics that we take into account in this work. We correspondingly modify the public BBN codes, **ParthENoPE** and **AlterBBN**, to implement the extended cosmological model.

### A. BBN as the primordial nuclear reactor

The Universe had cooled to temperatures below  $10^{10}$  K in about 1 s after the Big Bang [53]. At this epoch, the rate of weak interactions responsible for neutron–proton conversion started to fall below the Hubble expansion rate, leading to the freeze-out of the neutron-to-proton ratio,  $n/p$  [54]. After freeze-out, beta decays of free neutrons slightly decreased the ratio to  $n/p \approx 1/7$ , setting the stage for nucleosynthesis [5].

The first few reactions in the nuclear chain are concerned with the synthesis of deuterium via  $p+n \leftrightarrow d+\gamma$ , which had to overcome the so-called deuterium bottleneck due to the huge number of photons at  $T \gtrsim 0.1$  MeV. Only at lower temperatures can deuterium be massively produced, and a rapid sequence of BBN reactions then commenced. These reactions efficiently converted nearly all available neutrons into helium-4 ( ${}^4\text{He}$ ) within three minutes after the Big Bang, since it is the most tightly bound nuclide among light elements [55]. The primordial helium abundance expressed in terms of the (approximate) mass fraction,  $Y_{\text{P}} \equiv 4n_{{}^4\text{He}}/n_{\text{b}}$ , is thus primarily determined by the neutron-to-proton ratio at freeze-out;  $Y_{\text{P}} \simeq 0.25$  in standard BBN. Here  $n_{\text{b}}$  is the total number density of baryons. Other light nuclides are synthesized at the same time, including helium-3 and lithium-7.

In standard BBN, the final values of the light element abundances are sensitive to two physical parameters: (i) the baryon-to-photon ratio,  $\eta \equiv n_{\text{b}}/n_{\gamma}$ , and (ii) the free neutron lifetime,  $\tau_n$ . The baryon-to-photon ratio describes the baryon density of the Universe. A higher value of  $\eta$  leads to more efficient deuterium burning, resulting in a lower primordial deuterium abundance,  $\text{D}/\text{H} \equiv n_{\text{D}}/n_{\text{H}}$  [4, 7]. Meanwhile, the longer the neutron lifetime, the higher the value of  $n/p$  due to fewer decays and hence higher  $Y_{\text{P}}$ . Therefore, even though these two parameters are well measured by other astronomical observations or laboratory experiments [56, 57], BBN provides an independent verification.

## B. Nuclear network and differential equations

Modern BBN calculations are computationally intensive due to the need to evolve an extensive nuclear reaction network, often composed of tens of nuclear species linked by over a hundred reactions [11]. For example, `PARthENoPE` and `AlterBBN` consider the same 100 reactions for 26 nuclides [27, 30], while `PRIMAT` evolves as many as 391 reactions for 59 nuclides [13, 32]. In each BBN code, the corresponding system of coupled ODEs is integrated to obtain the primordial element abundances. Defining  $Y_i \equiv n_i/n_b$  for the  $i$ th nuclear species ( $n_i$  is its number density), one can express the general form of the ODE that describes a reaction in the network as

$$\dot{Y}_{i_1} = \sum_{i_2 \dots i_p, j_1 \dots j_q} N_{i_1} \left( \Gamma_{j_1 \dots j_q \rightarrow i_1 \dots i_p} \frac{Y_{j_1}^{N_{j_1}} \dots Y_{j_q}^{N_{j_q}}}{N_{j_1}! \dots N_{j_q}!} - \Gamma_{i_1 \dots i_p \rightarrow j_1 \dots j_q} \frac{Y_{i_1}^{N_{i_1}} \dots Y_{i_p}^{N_{i_p}}}{N_{i_1}! \dots N_{i_p}!} \right), \quad (1)$$

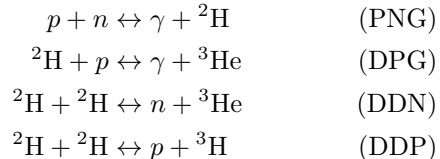
without restricting to two-body reactions [32, 36]. Here  $N_i$  is the stoichiometric coefficient of species  $i$  (the number of the  $i$ th nuclide) in the reaction and  $\Gamma_{i_1 \dots i_p \rightarrow j_1 \dots j_q}$  denotes the nuclear reaction rates, proportional to the thermally averaged cross sections,  $\langle \sigma v \rangle$ . Eq. (1) results from the Boltzmann equation. Nontrivial phases in the thermal history of the early Universe, such as electron-positron annihilation and neutrino decoupling, affect the nuclear network via the energy densities of relevant species and the Hubble expansion rate [25, 58].

The resulting system of ODEs is highly stiff because the timescales of nuclear reactions span many orders of magnitude [33]. Its numerical integration requires extremely small step sizes when rapid burning occurs, which is otherwise suboptimal for accurately resolving slower weak interactions at the onset of BBN calculations [5, 32]. In the meantime, stringent tolerance is needed to avoid secular drifts in the predicted abundances. Furthermore, each integration step often involves repeated interpolations of a grid of reaction rates and an implicit solution to the temperature-entropy evolution [5, 25, 32]. Hence, all of the above factors and the sheer dimensionality of the network combine to make traditional first-principles BBN computations exceedingly time-consuming [28]. This motivates our deep learning emulator approach.

## C. BBN codes and cosmological model

In this work, we use the public BBN codes `PARthENoPE` v3.0 and `AlterBBN` v2.2 to generate training data for our emulator [29, 31]. To ensure a consistent implementation of nuclear physics, both codes are modified to use identical reaction rates for the following key reactions that

strongly impact  $Y_P$  and D/H:



These processes dominate the synthesis of deuterium and  ${}^4\text{He}$  during BBN, contributing to most of the theoretical uncertainties on D/H and  $Y_P$  [12, 21]. We consider the theoretical PNG rate calculated in Ref. [59], which is adopted by `AlterBBN`. For the other three reaction rates, we adopt the high-precision fits used by `PARthENoPE` based on the compilation of experimental data in Ref. [24], which includes the recent LUNA results on the DPG rate [20].

The resulting primordial element abundances from BBN calculations depend on the cosmological model; they can be sensitive to parameters of both the standard  $\Lambda$ CDM model and extended scenarios. Regarding the former, both `PARthENoPE` and `AlterBBN` take as input the baryon-to-photon ratio,  $\eta$ , or  $\eta_{10} \equiv \eta \times 10^{10}$ . It is equivalent to the cosmic baryon density,  $\Omega_b h^2$ , according to [5]

$$\eta_{10} = 273.3036 \Omega_b h^2 (1 + 7.16958 \times 10^{-3} Y_P). \quad (2)$$

We apply this relationship to convert between  $\Omega_b h^2$  and  $\eta_{10}$  (or  $\eta$ ) in our modifications of both BBN codes.

For BSM scenarios, the extra relativistic degrees of freedom are parameterized by  $\Delta N_{\text{eff}}$  as usual, while the standard effective number of relativistic species is  $N_{\text{eff}}^{\text{SM}} = 3.044$ , accounting for the three neutrinos in the Standard Model (SM) [60–62]. In addition, we consider a possible pre-BBN kination/stiff phase. The energy density of a stiff fluid redshifts as  $a^{-6}$  so that the universe transitions from the stiff phase to the radiation-dominated (RD) era at early times. Following Refs. [44, 63], this stiff-to-radiation transition is parameterized by the ratio of the stiff-fluid energy density to the photon energy density at  $T_{10} \equiv 10 \text{ MeV}$ ,

$$\kappa_{10} \equiv \left( \frac{\rho_s}{\rho_\gamma} \right)_{T=10 \text{ MeV}}. \quad (3)$$

The impacts of a stiff phase on the primordial element abundances are previously examined by some of us in Refs. [50, 64, 65].

In this work, we use  $\Delta N_{\text{eff}}$  and  $\kappa_{10}$  as free parameters. Our modified `PARthENoPE` takes them as input parameters directly. On the other hand, to adapt to the code structure of `AlterBBN`, our modified version of `AlterBBN` describes the extra radiation and the stiff phase by equivalent input parameters  $\kappa_{\text{rad}, i}$  and  $\kappa_{s, i}$ , respectively. They are defined as

$$\kappa_{\text{rad}, i} \equiv \Delta N_{\text{eff}} \cdot \frac{7}{8} \left( \frac{4}{11} \right)^{4/3} \left( \frac{T_{\text{CMB}}}{T_i a_i} \right)^4, \quad (4)$$

$$\kappa_{s, i} \equiv \kappa_{10} \cdot \left( \frac{10 \text{ MeV}}{T_i} \right)^4 \left( \frac{a_{10}}{a_i} \right)^6, \quad (5)$$

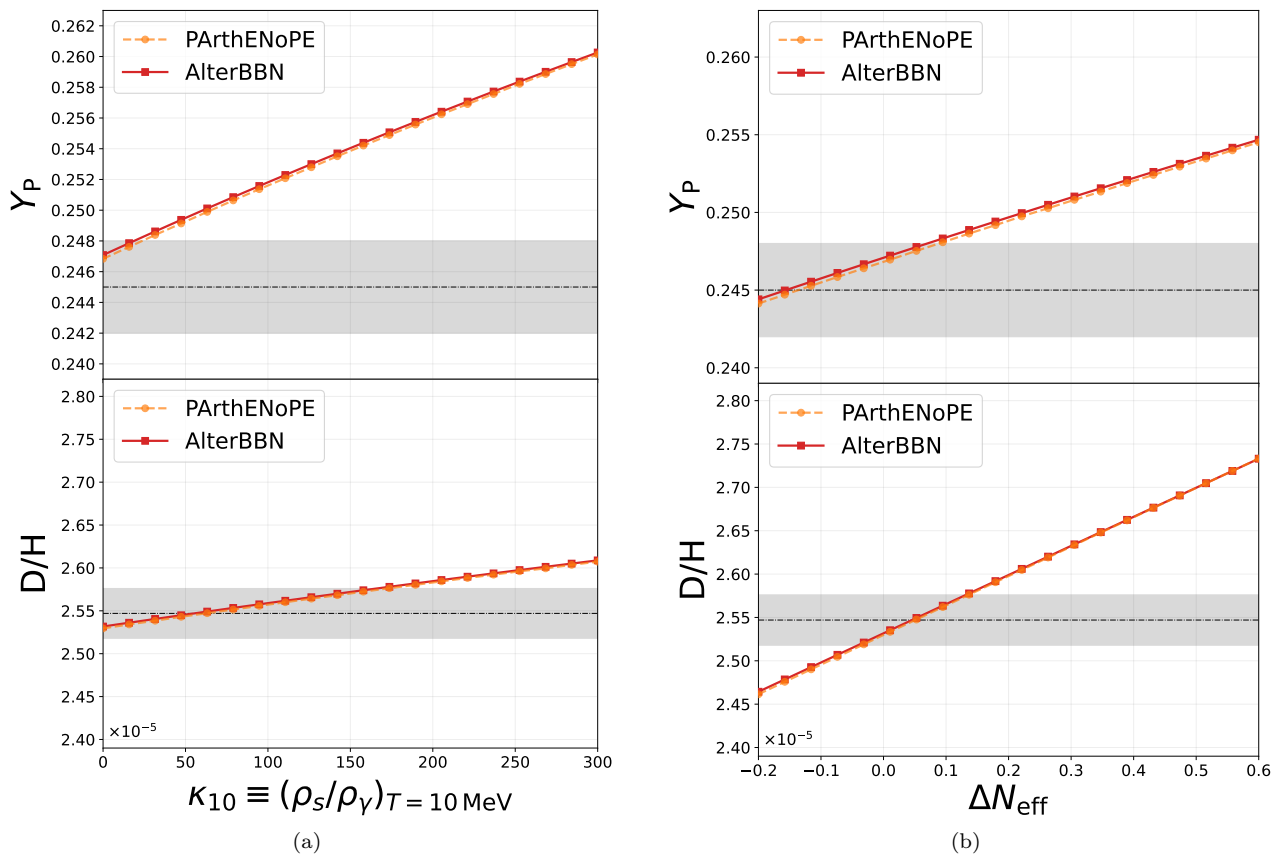


FIG. 1. Consensus of primordial element abundances computed by our modified PARthENoPE (orange dashed lines with circle markers) and AlterBBN (red solid lines with square markers). Each panel contains two stacked subplots for  $Y_P$  and  $D/H$ , respectively. Fig. 1a displays their relations with the density parameter of the stiff fluid,  $\kappa_{10} \equiv (\rho_s/\rho_\gamma)_{T=10 \text{ MeV}}$ , while Fig. 1b shows the relations with the effective number of extra relativistic species,  $\Delta N_{\text{eff}}$ . The gray shaded bands denote the  $1\sigma$  observational constraints from Ref. [66] and the black dashed lines mark the corresponding central values.

where  $T_i = 27 \times 10^9 \text{ K}$  is the initial temperature of AlterBBN calculations [31],  $T_{\text{CMB}} = 2.7255 \text{ K}$  is the observed temperature of the cosmic microwave background (CMB) today [67],  $a_i$  and  $a_{10}$  denote the scale factors at  $T_i$  and  $T_{10}$ , respectively. These parameters measure the energy density ratios of each BSM component to photons at  $T_i$  when AlterBBN starts its integration. Eqs. (4) and (5) are used to convert between  $(\Delta N_{\text{eff}}, \kappa_{10})$  and  $(\kappa_{\text{rad}, i}, \kappa_{\text{s}, i})$  for AlterBBN. Our modified BBN codes are publicly available at the links in Refs. [68, 69].

In summary, we consider four free physical parameters,  $\Omega_b h^2$ ,  $\tau_n$ ,  $\Delta N_{\text{eff}}$  and  $\kappa_{10}$ . Their ranges are listed in Table I. The bounds on  $\Omega_b h^2$  and  $\tau_n$  are chosen in accordance with their current measured values [56, 57]. The range of  $\Delta N_{\text{eff}}$  formally allows for negative values for completeness. Negative  $\Delta N_{\text{eff}}$  might occur in non-standard scenarios, e.g., in which the temperature of the SM neutrinos is lower than expected.

For illustration purposes, we present the dependences of the predicted  $Y_P$  and  $D/H$  on  $\kappa_{10}$  and  $\Delta N_{\text{eff}}$  in Fig. 1. The results are based on our modified BBN codes, PARthENoPE and AlterBBN. The coincidence of the two curves in each panel shows that the two solvers yield

TABLE I. Free parameters of BBNNet and their ranges. Eqs. (2), (4) and (5) are used to convert these parameters to the intrinsic input of PARthENoPE and AlterBBN when necessary.

Parameter	Range
$\Omega_b h^2$	[0.005, 0.1]
$\tau_n$ (s)	[875.5, 884.5]
$\Delta N_{\text{eff}}$	[-1.0, 1.0]
$\kappa_{10}$	[0, 1000]

nearly identical primordial abundances across the explored parameter ranges, demonstrating the consistency between our implementations of the same BSM physics in the two codes.

### III. METHODOLOGY: DATA GENERATION AND EMULATOR DESIGN

Our neural network emulator, BBNNet, is trained on the input parameters and the output data of our modi-

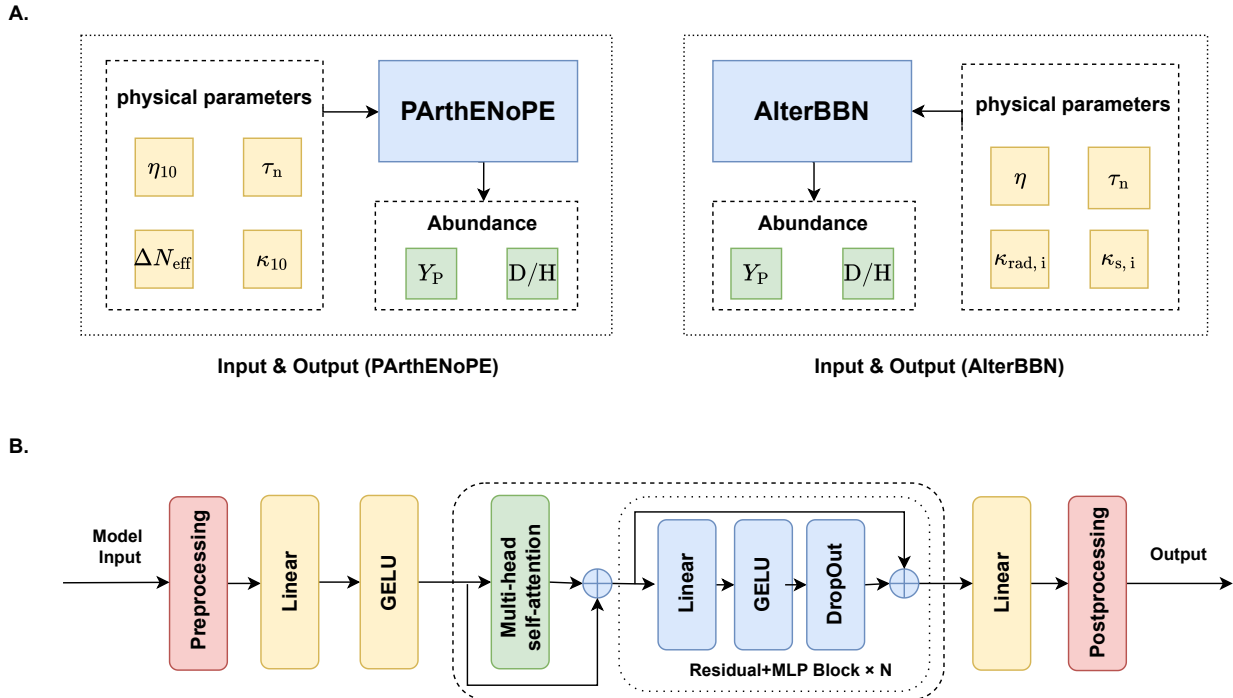


FIG. 2. Overview of the BBNNet emulator and its training interface. Panel A shows the input–output schematic for the two BBN solvers used to generate the training set. Each solver takes as input the baryon density  $\Omega_b h^2$ , the neutron lifetime  $\tau_n$ , and any beyond-standard-model extensions. For scenarios with a stiff-fluid sector, the solvers parameterize this component through  $\kappa_{10}$ , defined as the stiff-fluid to photon energy-density ratio at  $T = 10$  MeV. The solvers encode relativistic-sector modifications either through  $\Delta N_{\text{eff}}$  or through generalized coefficients  $\kappa_{\text{rad},i}$ . They then return the primordial abundances  $Y_P$  and D/H for comparison with observations. Panel B depicts the BBNNet architecture. The network projects the inputs with a linear–GELU layer, applies a multi-head self-attention module, and processes the result through  $N$  residual MLP blocks. It finally uses a linear head to predict  $(Y_P, D/H)$ .

fied BBN codes described above. The current version of BBNNet predicts only the well-measured  $Y_P$  and D/H, to be ready for the next-stage likelihood analysis. However, it can be easily generalized to predict the primordial abundances of other light elements from first-principles BBN calculations.

In this section, we describe our methodology for constructing BBNNet, including a robust strategy for data generation and a customized design of the neural network architecture. Our method can also be applied to emulate other generic BBN codes.

### A. Data generation strategy

We generate separate training and validation data sets using each of the two BBN codes, PARthENoPE and AlterBBN. They are treated as the ground truth for our neural networks. We sample the four physical parameters listed in Table I, assuming uniform priors on  $\Omega_b h^2$ ,  $\Delta N_{\text{eff}}$  and  $\tau_n$ , and a log-uniform prior on  $\kappa_{10}$  [70]. To ensure uniform sampling in the multidimensional parameter space, we use the Latin hypercube sampling method

[71, 72]. The parameters are subsequently converted to the intrinsic input of PARthENoPE and AlterBBN when necessary, using Eqs. (2), (4) and (5). The data generation pipeline is illustrated in Fig. 2A.

All BBN computations are performed on Intel Xeon Gold CPUs. For PARthENoPE, we adopt its “complete” nuclear reaction network (26 nuclides, 100 reactions) to generate the data set [27], which costs  $\sim 20 - 30$  s (wall time, hardware-dependent) for a single run. For AlterBBN, we choose an ODE solver based on the second-order Runge-Kutta algorithm with half step test (setting “failsafe=7” in AlterBBN; see [31]), dubbed “RK2\_halfstep” throughout the paper. This algorithm results in an average wall time per run of  $\gtrsim 15$  s. The final data set contains 20,000 samples for each BBN code. Note that the distributions of the two data sets are different from each other, because a considerable part of the parameter space (specified by Table I) is not accepted by PARthENoPE as input, while AlterBBN accepts all combinations of the parameters within their prior ranges. For both data sets, we adopt the standard 8 : 1 : 1 split to obtain training, validation, and test data.

## B. Neural network architecture and data processing

BBNet is designed to ingest the four-dimensional vector of  $(\Omega_b h^2, \tau_n, \Delta N_{\text{eff}}, \kappa_{10})$  and output the primordial element abundances,  $(Y_P, D/H)$ . Its overall neural network architecture is illustrated in Fig. 2B. All input and output variables are transformed and standardized to have zero mean and unit variance before training, indicated by the preprocessing and postprocessing modules. These data projection techniques help BBNet learn patterns in the dependence of output on input with balanced weights, hence achieving a more efficient training process and increasing the accuracy of the resultant model.

As shown in Fig. 2B, the preprocessed input data are reshaped into 4096-dimensional vectors via a linear projection. They are then passed through a Gaussian Error Linear Unit (GeLU) activation function [73]. These two layers can be expressed together as

$$h_0 = \text{GeLU}(W_{\text{lin}} X_{\text{scaled}} + b_{\text{lin}}), \quad (6)$$

where  $W_{\text{lin}}$  and  $b_{\text{lin}}$  are learnable weights and bias parameters in the linear projection layer.

We employ a multi-head self-attention (MHSA) module to further reparameterize the data [43]. The MHSA module can dynamically rescale the relative contributions of the physical parameters. We use eight attention heads, with the MHSA operation defined as

$$\text{MHSA}(h_0) = \text{Concat}(\text{head}_1, \dots, \text{head}_8) W_O, \quad (7)$$

where each head is computed as

$$\text{head}_i = \text{softmax}\left(\frac{Q_i K_i^T}{\sqrt{d_k}}\right) V_i. \quad (8)$$

Here  $Q_i$ ,  $K_i$ , and  $V_i$  denote the linear projections learned from the input  $h_0$ , and  $d_k$  is the key dimension, included as a scaling factor to stabilize the softmax layer [43]. The MHSA module is implemented with a residual connection:

$$h_1 = h_0 + \text{MHSA}(h_0). \quad (9)$$

We then take  $h_1$  to initialize the residual multilayer perceptron (MLP) stack with  $N$  blocks, expressed as:

$$h_{t+1} = h_t + \text{Dropout}\left(\text{GELU}(h_{t+1} W_t + \mathbf{b}_t)\right), \quad (10)$$

where  $W_t$  and  $\mathbf{b}_t$  are the learnable parameters of the  $t$ -th MLP block,  $t = 1, \dots, N$ . A dropout rate of 0.3 is used to regularize training and mitigate overfitting [74].

Finally, another linear projection layer transforms the 4096-dimensional data vectors to the predicted abundances  $(Y_P, D/H)$ , up to a postprocessing step.

## IV. BBNET TRAINING AND VALIDATION

This section details the training strategy of BBNet, which is proven to be successful and stable on both data sets (generated by PathENoPE and AlterBBN). Our techniques here can be generalized to train emulators for other BBN codes.

### A. Optimizer and scheduler

The BBNet model is trained using the AdamW optimizer. It combines the adaptive learning rate advantages of the Adam optimizer with decoupled weight decay [75, 76]. For both data sets, the initial learning rate is set to  $5 \times 10^{-5}$ , with a weight decay parameter  $\lambda_W = 10^{-5}$ . To avoid exploding gradients, we apply gradient clipping with a maximum norm threshold of 1.0.

We adopt a batch size of 16 for each iteration of the training processes. This batch size balances computational costs (GPU memory) and model complexity. We employ a scheduler that reduces the learning rate by a factor of 0.5 whenever the validation loss stops improving for 10 consecutive epochs. This strategy promotes rapid initial convergence and allows for finer parameter adjustments once the model begins to plateau.

### B. Regularization

During training and validation, we apply several regularization techniques to mitigate overfitting and improve the generalizability of the model to unseen data. Dropout is implemented by randomly setting a fraction of activations to zero. It discourages complex coadaptations between neurons, so that the model is inclined to learn more robust features. Weight decay is integrated through the AdamW optimizer, as mentioned above. This operation further enhances the stability of the model by suppressing large weights and favoring simpler representations.

We use the standard mean absolute error (MAE) for the loss function. We also include a regularization term that enforces the local stability of model predictions under small perturbations of the input parameters. It penalizes the differences between the model outputs at  $\mathbf{x}$  and  $\mathbf{x} + \boldsymbol{\epsilon}$  (here  $\boldsymbol{\epsilon}$  denotes a Gaussian perturbation), expressed as follows:

$$\mathcal{L}_{\text{smooth}} = \mathbb{E}_{\boldsymbol{\epsilon} \sim \mathcal{N}(\mathbf{0}, \sigma^2 \mathbf{I})} \|f(\mathbf{x} + \boldsymbol{\epsilon}) - f(\mathbf{x})\|_2^2, \quad (11)$$

where  $\|\cdot\|_2$  is the Euclidean norm of the output vector and  $\sigma = 0.02$  is fixed in all reported experiments. This term suppresses fluctuations in the learned mapping, guaranteeing smooth responses to input parameters.

In addition, we introduce another degree of regularization in terms of the following symmetric mean absolute percentage error (sMAPE) concerning the deuterium

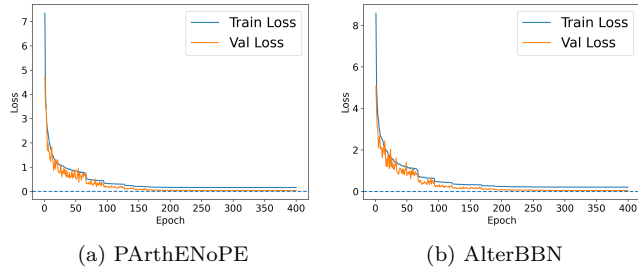


FIG. 3. Training and validation loss curves for the BBNet emulators. Figs. 3a and 3b illustrate the training processes of the neural network models based on data sets obtained by our modified PArthENoPE and AlterBBN, respectively. The loss function is defined as the mean absolute error between the predicted and true values of  $(Y_P, D/H)$ . Both losses decrease rapidly and stabilize within 300 epochs, reaching values close to zero with no indications of overfitting.

abundance:

$$\mathcal{L}_{\text{sMAPE}} = \frac{1}{N} \sum_{i=1}^N \frac{2 | \hat{y}_{D/H,i}^{(\text{raw})} - y_{D/H,i}^{(\text{raw})} |}{| \hat{y}_{D/H,i}^{(\text{raw})} | + | y_{D/H,i}^{(\text{raw})} |}. \quad (12)$$

This term helps the model achieve the desired accuracy in the predicted values of  $D/H$ , which span many orders of magnitude in our data sets.

### C. Training and validation loss

The total objective function combines the MAE loss (weighted between  $Y_P$  and  $D/H$ ) and the two regularization terms described above. It is formally written as

$$\mathcal{L}_{\text{total}} = \mathcal{L}_{\text{MAE}} + \lambda_{\text{smooth}} \mathcal{L}_{\text{smooth}} + \lambda_{D/H} \mathcal{L}_{\text{sMAPE}}, \quad (13)$$

where  $\lambda_{\text{smooth}}$  and  $\lambda_{D/H}$  are hyperparameters. We set  $\lambda_{\text{smooth}} = 0.1$  and  $\lambda_{D/H} = 50$ .

The loss curves for training and validation are presented in Fig. 3 for both BBNet models. The convergence of the two training processes confirms the stability of the neural network models and the generalizability of our framework. The closeness of the training and validation curves for both data sets demonstrates that our BBNet models have achieved optimal complexity.

## V. RESULTS

We perform a comprehensive twofold evaluation of the trained BBNet emulators to verify both its predictive accuracy and computational efficiency. In Sec. V A, we quantitatively benchmark the emulator predictions against the ground-truth outputs of the underlying BBN codes. We also compare them with the current observational constraints on  $Y_P$  and  $D/H$ . Subsequently,

Sec. V B explores the dependence of the predicted primordial abundances on the physical parameters over their most relevant ranges.

### A. Emulation accuracy and efficiency

We first assess the performance of BBNet by its accuracy in reproducing the results of BBN calculations. For both test sets generated by PArthENoPE and AlterBBN, the BBNet emulator accurately reproduces the true values of  $Y_P$  and  $D/H$ , as illustrated in Fig. 4. Note that AlterBBN can output small  $D/H$  values ( $< 10^{-5}$ ) while PArthENoPE only allows for values of the same order as the measured deuterium abundance (see the upper right panel of Fig. 4). Hence, to achieve the desired accuracy in predicting small values of  $D/H$  produced by AlterBBN, our corresponding BBNet emulator trains distinct models (expert modes) for two ranges of  $D/H$ ,  $[10^{-7}, 10^{-5}]$  and  $[10^{-5}, 10^{-3}]$ , respectively (see Appendix A for details).

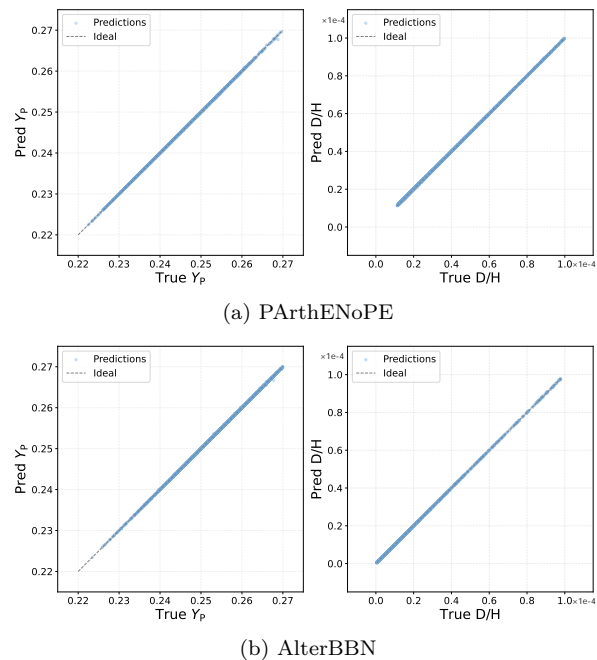


FIG. 4. Comparison between the primordial element abundances predicted by BBNet and the ground truth. Each panel compares BBNet predictions on the vertical axis with outputs of the benchmark solver on the horizontal axis. Fig. 4a shows results based on PArthENoPE using its complete network. Fig. 4b shows results based on AlterBBN with its RK2\_halfstep mode. Each subpanel presents  $Y_P$  on the left and  $D/H$  on the right, where blue scatter points denote individual test samples plotted against the corresponding solver values. The diagonal dashed line in each plot indicates ideal emulation with  $\hat{y} = y$ .

In all cases illustrated in Fig. 4, the close agreement between predictions and ground-truth values demonstrates that the BBNet framework is not confined to the internal implementation of any single BBN solver. Instead, it

effectively learns the underlying functional dependence between the physical parameters and primordial light element abundances.

To further quantify this agreement, we evaluate two complementary regression metrics that characterize both the magnitude and the direction of residual errors. First, the mean percentage error (MPE) measures the average signed relative difference between the predicted and the true abundances, defined as

$$\text{MPE} = \frac{1}{N} \sum_{i=1}^N \frac{\hat{y}_i - y_i}{y_i} \times 100\%. \quad (14)$$

We also consider the root mean square percentage error (RMSPE) that describes the absolute magnitude of relative errors as follows:

$$\text{RMSPE} = \sqrt{\frac{1}{N} \sum_{i=1}^N \left( \frac{\hat{y}_i - y_i}{y_i} \times 100\% \right)^2}. \quad (15)$$

Regarding observational constraints on the primordial abundances, we adopt the values reported by the most recent Review of Particle Physics (2025) as the benchmark here [66],

$$\begin{aligned} Y_{\text{P}} &= 0.245 \pm 0.003, \\ D/H &= (2.547 \pm 0.029) \times 10^{-5}. \end{aligned} \quad (16)$$

These values were compiled from a group of astronomical measurements, e.g., Refs. [77–83] for  $Y_{\text{P}}$  and Refs. [23, 84–89] for  $D/H$ .

We summarize the quantitative results of emulator performance in Table II using the metrics defined above. Both the RMSPE and the MPE values are far below the observational uncertainties—by more than four orders of magnitude for  $Y_{\text{P}}$ —demonstrating that **BBNet** accurately reproduces the theoretical values of  $Y_{\text{P}}$  and  $D/H$  with negligible errors. **BBNet** is therefore a fully competent alternative to BBN codes for parameter inference tasks.

TABLE II. Comparison of RMSPE, MAPE, and MPE (%) for **BBNet** trained on two BBN solvers, evaluated against their respective ground truths.

Abundance	RMSPE (%)	MAPE (%)	MPE (%)
<i>PARthENoPE</i>			
$Y_{\text{P}}$	0.0158	0.0064	−0.0011
$D/H$	0.0503	0.0331	0.0013
<i>AlterBBN</i>			
$Y_{\text{P}}$	0.0175	0.0055	−0.0014
$D/H$	0.0799	0.0455	0.0002

In addition to the accuracy of model predictions, computational efficiency is equally critical for applications that require large-scale evaluations. Fig. 5 compares the latency (wall time) per execution between different methods. On both CPUs and GPUs, **BBNet** achieves an average speed-up of several orders of magnitude relative

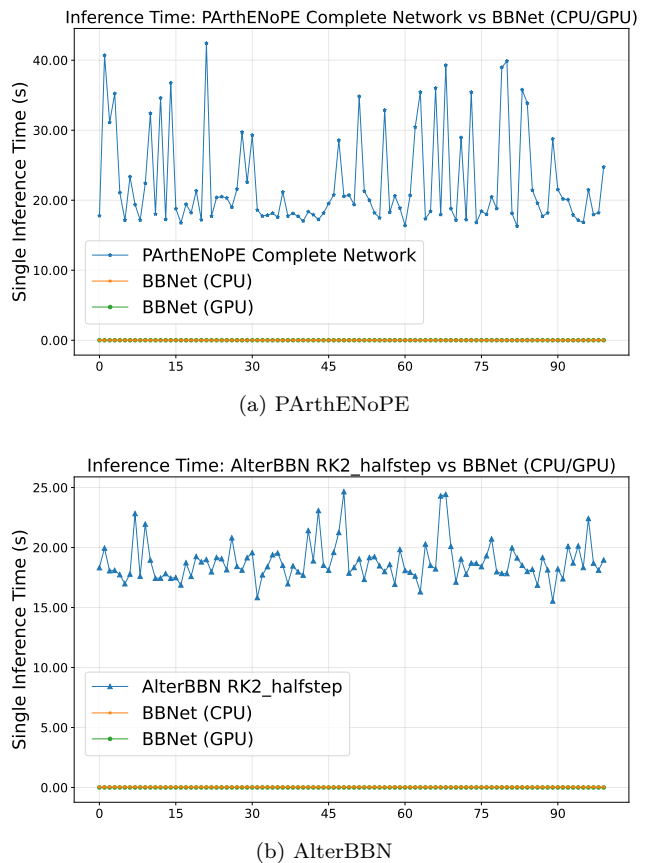


FIG. 5. Single-sample inference times for BBN numerical solvers and the **BBNet** emulator. The wall times are measured for 100 samples for each method. Blue lines indicate the runtimes of the baseline solvers, namely the complete network **PARthENoPE** (Fig. 5a) and **AlterBBN** with the `RK2_halfstep` mode (Fig. 5b). Orange and green lines show the corresponding inference times of the **BBNet** emulator executed on CPU and GPU, respectively. The emulator achieves a speed-up of  $\sim 10^3 - 10^4$  times in both cases and attains sub-millisecond evaluations on GPU with minimal overhead on CPU.

to traditional ODE-based solvers. This dramatic acceleration enables real-time parameter estimation using MCMC sampling, where millions of abundance evaluations are typically required.

## B. Dependence of primordial abundances on physical parameters

Here we demonstrate the accuracy of **BBNet** emulations from another perspective, the dependence of  $Y_{\text{P}}$  and  $D/H$  on the physical parameters. Using the test sets in both cases (**PARthENoPE** and **AlterBBN**), we compare the predicted element abundances with those obtained by the BBN calculations. As illustrated in Figs. 6 and 7, each parameter is individually varied while the others are fixed at their fiducial values:  $\kappa_{10} = 0.0$ ,  $\Delta N_{\text{eff}} = 0.0$ ,  $\Omega_b h^2 = 0.02237$  [56], and  $\tau_n = 879.4$  s [66]. Our results

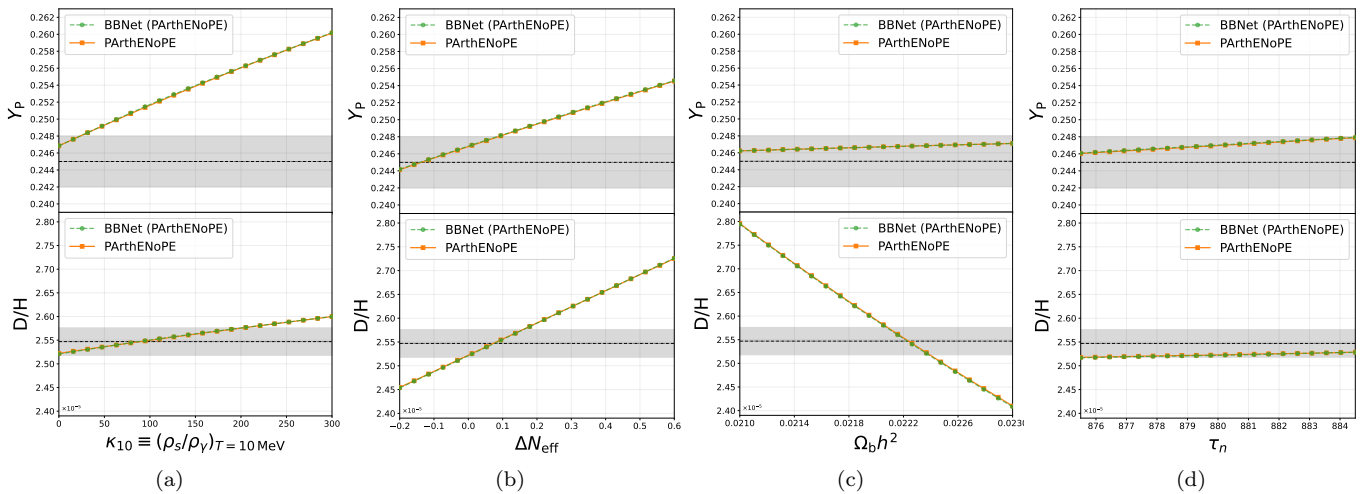


FIG. 6. Parameter dependence of primordial abundances from PARthENoPE and BBNet. The top axes show the dependence of the primordial helium mass fraction  $Y_{\text{P}}$ , and the bottom axes show the dependence of the deuterium-to-hydrogen ratio  $D/H$ . Predictions from PARthENoPE appear as solid curves with circle markers, and the BBNet emulator appears as dashed curves with circle markers. Fig. 6a varies the density parameter of the stiff fluid,  $\kappa_{10}$ . Fig. 6b varies  $\Delta N_{\text{eff}}$ , Fig. 6c varies the baryon density  $\Omega_{\text{b}} h^2$ , and Fig. 6d varies the neutron lifetime  $\tau_n$ . In each case, all remaining cosmological and nuclear inputs are held fixed at their fiducial values. Gray shaded bands show the one-sigma observational intervals adopted from Ref. [66]. Black dashed lines indicate the corresponding central values.

show a perfect agreement between the first-principles computations and the neural network emulations over large variations in the values of parameters.

In this work,  $\kappa_{10}$  and  $\Delta N_{\text{eff}}$  are the parameters that describe BSM physics. Their relationships with the primordial element abundances shown in Figs. 6 and 7 are essentially the same as those shown in Fig. 1. In particular,  $Y_{\text{P}}$  increases monotonically with  $\kappa_{10}$  and is highly sensitive to it, whereas the corresponding dependence of  $D/H$  on  $\kappa_{10}$  is comparatively weak. By contrast,  $\Delta N_{\text{eff}}$  strongly influences both abundances with a monotonically increasing trend. As for the SM sector, changes in the baryon density,  $\Omega_{\text{b}} h^2$ , induce negligible changes in  $Y_{\text{P}}$  but a significant, monotonically decreasing effect on  $D/H$ . Variations in the neutron lifetime, however, have small impacts on both  $Y_{\text{P}}$  and  $D/H$  with slightly increasing trends.

These results exhibit the robustness of BBNet in tasks that involve parameter sweeps, where rapid evaluations are essential. By retaining the outcomes of traditional numerical solvers while offering a speed-up of several orders of magnitude, BBNet enables efficient, bias-free cosmological inferences with BBN data, even when the prior ranges of parameters are wide.

## VI. COMPARISON BETWEEN BBNET EMULATIONS AND SIMPLIFIED BBN CALCULATIONS

Now that we have demonstrated the performance of our neural network emulator BBNet, in this section we

compare it with the traditional numerical approaches applied in existing parameter inference efforts, which must involve a trade-off between speed and accuracy. In fact, to allow for MCMC analyses that converge in reasonable hours, standard pipelines often rely on reduced nuclear networks or simplified ODE integrators. Although able to meet the working level of speed, these approximations may introduce systematic biases that can propagate into final inference results.

Here, we argue that the BBNet emulator renders this compromise obsolete. The assessment is carried out in two parts. In Sec. VIA we show that when applied to realistic MCMC sampling, the computational efficiency of BBNet exceeds those of simplified BBN calculations by orders of magnitude. Sec. VIB analyzes the error distributions that result from the two approaches. Systematic biases characteristic of simplified first-principles methods are not found in the BBNet results.

### A. Sampling efficiency in MCMC inferences

To quantify the computational acceleration provided by BBNet in a realistic setting, here we conduct benchmark tests for our emulator using MCMC sampling of a single chain with 1000 steps.

In the meantime, we choose commonly used configurations of PARthENoPE and AlterBBN as examples of simplified BBN calculations, which reflect the speed-accuracy trade-off. For PARthENoPE, we compare BBNet with its “small” network that takes into account 9 nuclides and 40 reactions only [27]. Recall that the corresponding

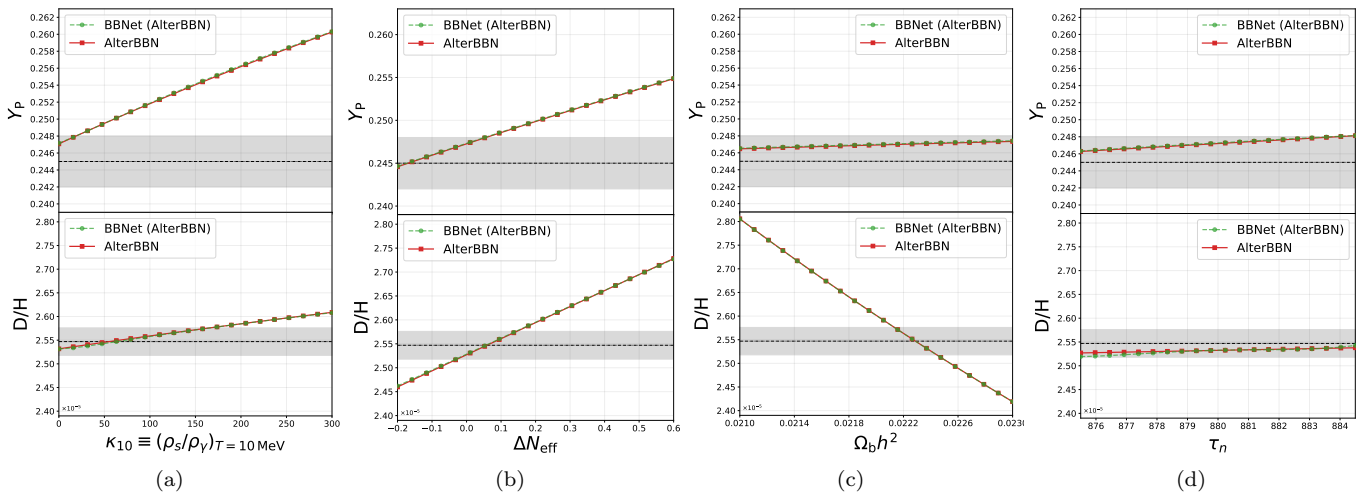


FIG. 7. Parameter dependence of primordial abundances from AlterBBN and BBNet. Similar to Fig. 6, the top panels show the dependence of  $Y_{\text{P}}$  and the bottom panels show the dependence of  $D/H$ . Each panel varies a single input parameter while all remaining inputs are fixed to the fiducial values. Horizontal gray bands denote the one-sigma observational intervals adopted from Ref. [66], and black dashed lines indicate the corresponding central values.

BBNet emulator reproduces results of the benchmark “complete” network. For AlterBBN, we contrast BBNet with the standard second-order Runge-Kutta method implemented in the code (setting “failsafe=3” in AlterBBN), dubbed “RK2” here [31]. This RK2 mode is faster but less accurate than the benchmark RK2\_halfstep mode to which we anchor the emulator.

Our results, summarized in Table III, demonstrate that BBNet provides the optimal solution with its tremendous advantage in computational efficiency. In this MCMC setting, the emulator achieves a speed-up of  $\gtrsim 10^3$  relative to the benchmark, full BBN methods (the complete network of ParthENoPE and the RK2\_halfstep mode of AlterBBN). More importantly, it outperforms the simplified methods by a factor of  $\mathcal{O}(10^2)$ . These findings render the reduced numerical methods unnecessary: BBNet is superior to the latter in both efficiency and accuracy. We further elaborate on the accuracy argument in the next subsection.

## B. Residual error distribution

As mentioned above, the speed-accuracy trade-off exploited by the simplified BBN methods often leads to systematic biases in the predicted abundances. In contrast, a robust emulator such as BBNet is designed to reproduce the ground truth of the full numerical calculations without introducing systematic shifts in residual errors. Using the same high-precision benchmarks, we analyze the distributions of residual errors in the results of both BBNet emulations and simplified calculations (the small network of ParthENoPE and the RK2 mode of AlterBBN). We evaluate the same metrics as above, e.g., MPE and RMSPE. The results are summarized in Table IV.

For the ParthENoPE data set (see the upper block of Table IV), BBNet shows a distinct advantage in eliminating systematic biases (described by MPE). The small network approximation introduces an average offset of  $\sim 0.08\%$  for  $D/H$ , a deviation that is consistent throughout the parameter space, while BBNet reduces the MPE to a negligible level (0.0013%).

The superiority of the emulator is further demonstrated by the comparison within the AlterBBN data set, as shown in the lower block of Table IV and Fig. 8. The faster but less accurate RK2 solver exhibits a considerable systematic drift, underestimating both  $Y_{\text{P}}$  and  $D/H$ . The error distributions of the BBNet predictions, conversely, are centered around zero (with MPEs  $\lesssim 10^{-3}\%$ ), as illustrated in Fig. 8. Thus, our emulator faithfully reproduces the solutions of the benchmark RK2\_halfstep method without inducing any systematic skew as does the RK2 integrator. In addition, BBNet also significantly reduces scatters in the error distributions, e.g., lowering the RMSPE in the  $D/H$  results by a factor of  $\sim 2.5$  relative to the RK2 solver. The emulator achieves an RMSPE of  $\sim 10^{-2}\%$  for both  $Y_{\text{P}}$  and  $D/H$ , two orders of magnitude smaller than the relative errors from astronomical measurements; cf. Eq. (16). Therefore, when applied to a likelihood analysis, BBNet can yield correct constraints on the physical parameters that are determined only by observational data without introducing any computational errors.

These results confirm that BBNet can supersede simplified numerical schemes to generate primordial element abundances. By efficiently reproducing the solutions of full BBN calculations with negligible systematic biases and scatter, the emulator serves as a promising tool for cosmological inferences.

TABLE III. Comparison of computational time costs between the numerical methods and BBNet in MCMC inferences.

Code	Steps	Chains	Total Inference Time (s)	Speed-up
<i>Comparison Group 1: PARthENoPE</i>				
PARthENoPE (complete network)	1000	1	16860.39	1×
PARthENoPE (small network)	1000	1	830.38	20.3×
BBNet Emulator (trained on PARthENoPE)	1000	1	2.29	$7.4 \times 10^3$
<i>Comparison Group 2: AlterBBN</i>				
AlterBBN (RK2_halfstep)	1000	1	21267.83	1×
AlterBBN (RK2)	1000	1	569.49	37.3×
BBNet Emulator (trained on AlterBBN)	1000	1	7.64	$2.7 \times 10^3$

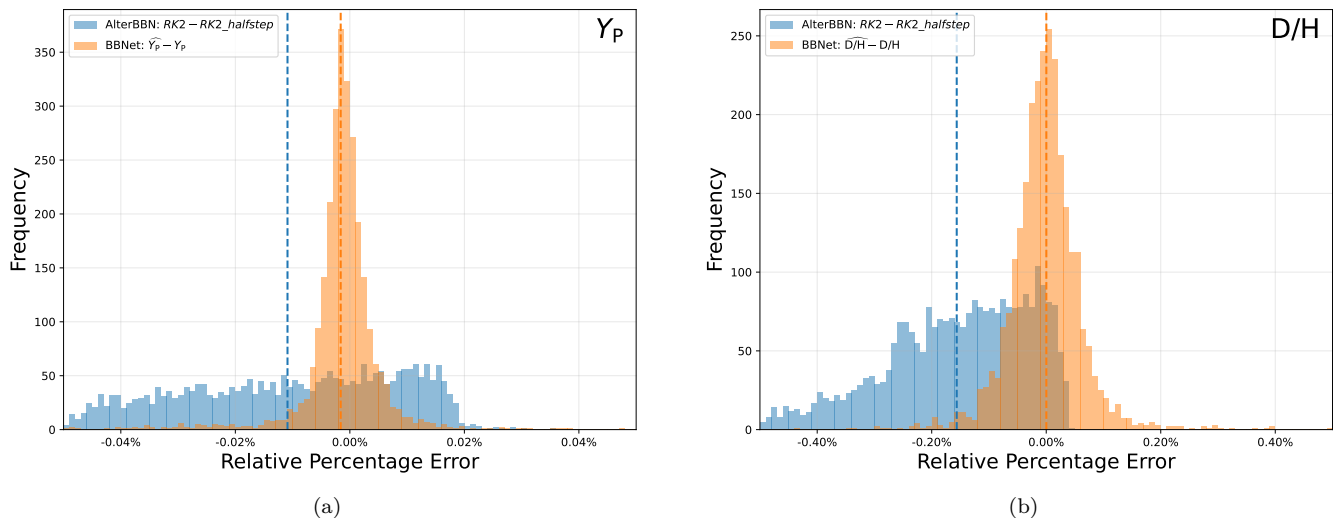


FIG. 8. Relative percentage error distributions in the AlterBBN test set. The left panel shows the errors for  $Y_P$ , and the right panel shows the errors for  $D/H$ . The errors are computed relative to the high-accuracy reference results obtained with the `RK2_halfstep` mode. Blue histograms show the residuals between the `RK2` mode and the standard `RK2_halfstep` reference. Orange histograms show the residuals between the BBNet predictions and the standard `RK2` mode, quantifying the emulator’s interpolation error. Dashed vertical lines in each color indicate the corresponding mean signed error. The horizontal axes are restricted to  $\pm 0.05\%$  for  $Y_P$  and  $\pm 0.5\%$  for  $D/H$  to resolve the fine structure of the distributions.

## VII. CONCLUSION

We have presented **BBNet**, a deep learning emulator designed to accelerate BBN calculations without compromising physical accuracy. The network employs a residual multi-head attention architecture to capture the non-linear dependencies of primordial abundances on physical parameters. We trained the model using Latin-hypercube samples derived from two independent BBN codes, **PARthENoPE** and **AlterBBN**, ensuring consistent treatments of nuclear physics between the two data sets. The physical parameters include those from the Standard Model as well as those that describe BSM physics, i.e., dark radiation and a stiff fluid.

Our results demonstrated that **BBNet** can effectively resolve the traditional trade-off between computational speed and theoretical accuracy. For both BBN codes, the emulator successfully reproduced the benchmark predic-

tions of the full numerical methods with negligible biases and scatter. Particularly, **BBNet** eliminated the systematic offsets inherent in simplified numerical calculations (such as the small network of **PARthENoPE**). In terms of efficiency, the emulator achieves a speed-up of  $\mathcal{O}(10^2)$  relative to the simplified methods and up to  $\mathcal{O}(10^4)$  compared with the full benchmark solvers. Based on these advantages, we advocate for the replacement of traditional approximate approaches by fast, high-fidelity neural network emulation.

In fact, the combination of accuracy and efficiency held by **BBNet** has removed the primary computational bottleneck in large-scale parameter inferences. **BBNet** provides an optimal solution to the forward modeling of primordial element abundances within Bayesian pipelines, enabling rigorous explorations of high-dimensional parameter spaces. Furthermore, our framework remains flexible: Unlike static interpolation tables, the network can be efficiently retrained to accommodate updated nuclear

TABLE IV. Relative percentage error metrics (mean, median, RMSPE) for the comparison between the numerical methods and the emulator, grouped by the data sets (PArthENoPE and AlterBBN).

Abundance	Models	Percentage Error (%)		
		Mean	Median	RMS
<i>PArthENoPE</i>				
$Y_{\text{P}}$	small network	-0.0083	-0.0083	0.0088
	BBNet	-0.0011	-0.0005	0.0158
D/H	small network	0.0768	0.0765	0.0771
	BBNet	0.0013	-0.0007	0.0503
<i>AlterBBN</i>				
$Y_{\text{P}}$	RK2	-0.0109	-0.0089	0.0221
	BBNet	-0.0016	-0.0011	0.0175
D/H	RK2	-0.1563	-0.1368	0.2033
	BBNet	0.0002	0.0014	0.0799

reaction rates or expanded prior ranges.

The BBNet framework presented here can be generalized to more detailed BBN studies, such as those involving nuclear reaction rates as free parameters or other BSM physics. Fast and accurate emulation of primordial element abundances will help shed light on the complex relationship between the BBN observables and any relevant physics, e.g., the *real* theoretical uncertainties due to poorly-determined nuclear rates (rather than computational errors). Meanwhile, we also plan to extend the emulator to predict the primordial abundances of helium-3 and lithium-7, which will facilitate a reexamination of the famous lithium problem. All source code, pretrained models, and data sets used in this work are publicly available at the link in Ref. [90].

## VIII. ACKNOWLEDGMENTS

F.Z. gratefully acknowledges the continuous support and valuable advice of the MIT LIGO Laboratory. This work was supported in part by the Ministry of Science and Technology of the People’s Republic of China (Grant No. 2023ZD0120704 under Project No. 2023ZD0120700) and by the National Natural Science Foundation of China (Grant No. 62372409). B.L. is supported by the Guangxi Key Research and Development Program (Guike FN2504240040), the Guangxi Natural Science Foundation (grant No. 2023GXNSFBA026114) and the National Natural Science Foundation of China (grant Nos. 12203012 and 12494575). Additional support was provided by the Guangxi Talent Program (“Highland of Innovation Talents”).

## Appendix A: Hierarchical Expert Mode for Adaptive Refinement

To address the wide dynamic range and complex distribution of the AlterBBN data set, we implement a two-stage hierarchical inference strategy. The architecture consists of a global *base* model, trained on the complete dataset, augmented by two domain-specialized *expert* models trained on filtered subsets of the parameter space. All three networks share an identical backbone architecture (`ResMLPWithAttn`). Each model checkpoint is stored alongside its corresponding normalization statistics (scalers) to ensure that the input-output transformations remain strictly reversible and consistent with the specific training distribution of each expert.

During the inference phase, the framework employs a hard-gating mechanism (activated via the `--exp` flag). The base model first generates a preliminary prediction,  $\widehat{D/H}_{\text{base}}$ . This value acts as a decision variable to route the input to the appropriate specialist network or to accept the base prediction, according to the following rule:

$$\widehat{D/H}_{\text{out}} = \begin{cases} \text{Expert 2} & \text{if } \widehat{D/H}_{\text{base}} \in [10^{-7}, 10^{-5}), \\ \text{Expert 1} & \text{if } \widehat{D/H}_{\text{base}} \in [10^{-5}, 10^{-3}], \end{cases} \quad (\text{A1})$$

For routed samples, the raw inputs are renormalized using the target expert’s specific statistics before being processed by the expert network. This band-specific renormalization is essential because the statistical moments of the filtered subsets differ significantly from the global distribution, and using global scalars for local experts would degrade precision.

We quantify the computational overhead of this approach in terms of per-sample wall-clock time and theoretical floating-point operations (FLOPs). In the AlterBBN test run ( $N = 3000$ ), the routing fraction is close to unity ( $f \approx 1$ ), which means that nearly all samples trigger a second forward pass. The resulting resource consumption is summarized in Table V. Since the expert mechanism requires loading up to three distinct sets of weights, the memory cost increases by a factor of  $\sim 3$  compared to the base-only mode, although this can be mitigated to  $\sim 2$  times via lazy loading.

TABLE V. Comparison of computational resources and latency between the *base-only* mode and the *expert* mode. Wall times are measured per sample over repeated trials. FLOPs are calculated for a single inference pass given the specific backbone configuration. The memory column reports the FP32 model weight footprint plus the storage required for the normalization scalars.

Inference Mode	Latency ( $\mu\text{s}$ )	FLOPs	Memory
Base only	36.5–56.2	$4.03 \times 10^8$	768 MiB
Expert mode	74.6–97.3	$8.05 \times 10^8$	2.25 GiB

- [1] R. A. Alpher and R. C. Herman, Remarks on the Evolution of the Expanding Universe, *Physical Review* **75**, 1089 (1949).
- [2] D. N. Schramm and M. S. Turner, Big-bang nucleosynthesis enters the precision era, *Rev. Mod. Phys.* **70**, 303 (1998).
- [3] B. D. Fields and K. A. Olive, Big bang nucleosynthesis, *Nucl. Phys. A* **777**, 208 (2006).
- [4] G. Steigman, Primordial Nucleosynthesis in the Precision Cosmology Era, *Annual Review of Nuclear and Particle Science* **57**, 463 (2007), arXiv:0712.1100 [astro-ph].
- [5] R. H. Cyburt, B. D. Fields, K. A. Olive, and T.-H. Yeh, Big bang nucleosynthesis: Present status, *Reviews of Modern Physics* **88**, 015004 (2016), arXiv:1505.01076 [astro-ph.CO].
- [6] B. D. Fields, K. A. Olive, T.-H. Yeh, and C. Young, Big-Bang Nucleosynthesis after Planck, *J. Cosmol. Astropart. P.* **2020**, 010 (2020), arXiv:1912.01132 [astro-ph.CO].
- [7] C. J. Copi, D. N. Schramm, and M. S. Turner, Big-Bang Nucleosynthesis and the Baryon Density of the Universe, *Science* **267**, 192 (1995), arXiv:astro-ph/9407006 [astro-ph].
- [8] F. Iocco, G. Mangano, G. Miele, O. Pisanti, and P. D. Serpico, Primordial nucleosynthesis: From precision cosmology to fundamental physics, *Phys. Rep.* **472**, 1 (2009), arXiv:0809.0631 [astro-ph].
- [9] M. Pospelov and J. Pradler, Big Bang Nucleosynthesis as a Probe of New Physics, *Annual Review of Nuclear and Particle Science* **60**, 539 (2010), arXiv:1011.1054 [hep-ph].
- [10] T.-H. Yeh, J. Shelton, K. A. Olive, and B. D. Fields, Probing physics beyond the standard model: limits from BBN and the CMB independently and combined, *J. Cosmol. Astropart. P.* **2022**, 046 (2022), arXiv:2207.13133 [astro-ph.CO].
- [11] R. V. Wagoner, W. A. Fowler, and F. Hoyle, On the Synthesis of Elements at Very High Temperatures, *Astrophys. J.* **148**, 3 (1967).
- [12] P. D. Serpico, S. Esposito, F. Iocco, G. Mangano, G. Miele, and O. Pisanti, Nuclear reaction network for primordial nucleosynthesis: a detailed analysis of rates, uncertainties and light nuclei yields, *J. Cosmol. Astropart. P.* **2004**, 010 (2004), arXiv:astro-ph/0408076 [astro-ph].
- [13] A. Coc, S. Goriely, Y. Xu, M. Saimpert, and E. Vangioni, Standard Big Bang Nucleosynthesis up to CNO with an Improved Extended Nuclear Network, *Astrophys. J.* **744**, 158 (2012), arXiv:1107.1117 [astro-ph.CO].
- [14] E. G. Adelberger, A. García, R. G. H. Robertson, K. A. Snover, A. B. Balantekin, K. Heeger, M. J. Ramsey-Musolf, D. Bemmerer, A. Junghans, C. A. Bertulani, J. W. Chen, H. Costantini, P. Prati, M. Couder, E. Uberseder, M. Wiescher, R. Cyburt, B. Davids, S. J. Freedman, M. Gai, D. Gazit, L. Gialanella, G. Imbriani, U. Greife, M. Hass, W. C. Haxton, T. Itahashi, K. Kubodera, K. Langanke, D. Leitner, M. Leitner, P. Vetter, L. Winslow, L. E. Marcucci, T. Motobayashi, A. Mukhamedzhanov, R. E. Tribble, K. M. Nollett, F. M. Nunes, T. S. Park, P. D. Parker, R. Schiavilla, E. C. Simpson, C. Spitaleri, F. Strieder, H. P. Trautvetter, K. Suemmerer, and S. Typel, Solar fusion cross sections. II. The pp chain and CNO cycles, *Reviews of Modern Physics* **83**, 195 (2011), arXiv:1004.2318 [nucl-ex].
- [15] Y. Xu, K. Takahashi, S. Goriely, M. Arnould, M. Ohta, and H. Utsunomiya, NACRE II: an update of the NACRE compilation of charged-particle-induced thermonuclear reaction rates for nuclei with mass number  $A \leq 16$ , *Nucl. Phys. A* **918**, 61 (2013), arXiv:1310.7099 [nucl-th].
- [16] C. Iliadis, K. S. Anderson, A. Coc, F. X. Timmes, and S. Starrfield, Bayesian Estimation of Thermonuclear Reaction Rates, *Astrophys. J.* **831**, 107 (2016), arXiv:1608.05853 [astro-ph.SR].
- [17] J. Moscoso, R. S. de Souza, A. Coc, and C. Iliadis, Bayesian Estimation of the  $D(p,\gamma)^3\text{He}$  Thermonuclear Reaction Rate, *Astrophys. J.* **923**, 49 (2021), arXiv:2109.00049 [astro-ph.CO].
- [18] G. Fiorentini, E. Lisi, S. Sarkar, and F. L. Villante, Quantifying uncertainties in primordial nucleosynthesis without Monte Carlo simulations, *Phys. Rev. D* **58**, 063506 (1998), arXiv:astro-ph/9803177 [astro-ph].
- [19] L. E. Marcucci, G. Mangano, A. Kievsky, and M. Viviani, Implication of the Proton-Deuteron Radiative Capture for Big Bang Nucleosynthesis, *Phys. Rev. Lett.* **116**, 102501 (2016), arXiv:1510.07877 [nucl-th].
- [20] V. Mossa, K. Stöckel, F. Cavanna, F. Ferraro, M. Aliotta, F. Barile, D. Bemmerer, A. Best, A. Boeltzig, C. Brogini, C. G. Bruno, A. Cacioli, T. Chillery, G. F. Ciani, P. Corvisiero, L. Csedreki, T. Davinson, R. Depalo, A. Di Leva, Z. Elekes, E. M. Fiore, A. Formicola, Z. Fülöp, G. Gervino, A. Guglielmetti, C. Gustavino, G. Gyürky, G. Imbriani, M. Junker, A. Kievsky, I. Kochanek, M. Lugaro, L. E. Marcucci, G. Mangano, P. Marigo, E. Masha, R. Menegazzo, F. R. Pantaleo, V. Patricchio, R. Perrino, D. Piatti, O. Pisanti, P. Prati, L. Schiavulli, O. Straniero, T. Szücs, M. P. Takács, D. Trezzi, M. Viviani, and S. Zavatarelli, The baryon density of the Universe from an improved rate of deuterium burning, *Nature (London)* **587**, 210 (2020).
- [21] T.-H. Yeh, K. A. Olive, and B. D. Fields, The impact of new  $d(p,\gamma)^3\text{He}$  rates on Big Bang Nucleosynthesis, *J. Cosmol. Astropart. P.* **2021**, 046 (2021), arXiv:2011.13874 [astro-ph.CO].
- [22] A. Coc, P. Petitjean, J.-P. Uzan, E. Vangioni, P. Descouvemont, C. Iliadis, and R. Longland, New reaction rates for improved primordial D/H calculation and the cosmic evolution of deuterium, *Phys. Rev. D* **92**, 123526 (2015), arXiv:1511.03843 [astro-ph.CO].
- [23] R. J. Cooke, M. Pettini, and C. C. Steidel, One Percent Determination of the Primordial Deuterium Abundance, *Astrophys. J.* **855**, 102 (2018), arXiv:1710.11129 [astro-ph.CO].
- [24] O. Pisanti, G. Mangano, G. Miele, and P. Mazzella, Primordial Deuterium after LUNA: concordances and error budget, *J. Cosmol. Astropart. P.* **2021**, 020 (2021), arXiv:2011.11537 [astro-ph.CO].
- [25] E. Grohs, G. M. Fuller, C. T. Kishimoto, M. W. Paris, and A. Vlasenko, Neutrino energy transport in weak decoupling and big bang nucleosynthesis, *Phys. Rev. D* **93**, 083522 (2016), arXiv:1512.02205 [astro-ph.CO].
- [26] M. Escudero, Neutrino decoupling beyond the Standard Model: CMB constraints on the Dark Matter mass with

- a fast and precise  $N_{eff}$  evaluation, *J. Cosmol. Astropart. P.* **2019**, 007 (2019), arXiv:1812.05605 [hep-ph].
- [27] O. Pisanti, A. Cirillo, S. Esposito, F. Iocco, G. Mangano, G. Miele, and P. D. Serpico, PARthENoPE: Public algorithm evaluating the nucleosynthesis of primordial elements, *Computer Physics Communications* **178**, 956 (2008), arXiv:0705.0290 [astro-ph].
- [28] R. Consiglio, P. F. de Salas, G. Mangano, G. Miele, S. Pastor, and O. Pisanti, PARthENoPE reloaded, *Computer Physics Communications* **233**, 237 (2018), arXiv:1712.04378 [astro-ph.CO].
- [29] S. Gariazzo, P. F. de Salas, O. Pisanti, and R. Consiglio, PARthENoPE revolutions, *Computer Physics Communications* **271**, 108205 (2022), arXiv:2103.05027 [astro-ph.IM].
- [30] A. Arbey, AlterBBN: A program for calculating the BBN abundances of the elements in alternative cosmologies, *Computer Physics Communications* **183**, 1822 (2012), arXiv:1106.1363 [astro-ph.CO].
- [31] A. Arbey, J. Auffinger, K. P. Hickerson, and E. S. Jenssen, AlterBBN v2: A public code for calculating Big-Bang nucleosynthesis constraints in alternative cosmologies, arXiv e-prints, arXiv:1806.11095 (2018), arXiv:1806.11095 [astro-ph.CO].
- [32] C. Pitrou, A. Coc, J.-P. Uzan, and E. Vangioni, Precision big bang nucleosynthesis with improved Helium-4 predictions, *Phys. Rep.* **754**, 1 (2018), arXiv:1801.08023 [astro-ph.CO].
- [33] A.-K. Burns, T. M. P. Tait, and M. Valli, PRyMordial: the first three minutes, within and beyond the standard model, *European Physical Journal C* **84**, 86 (2024), arXiv:2307.07061 [hep-ph].
- [34] N. Sabti, A. Magalich, and A. Filimonova, An extended analysis of Heavy Neutral Leptons during Big Bang Nucleosynthesis, *J. Cosmol. Astropart. P.* **2020**, 056 (2020), arXiv:2006.07387 [hep-ph].
- [35] L. Kawano, Let's go: Early universe 2. Primordial nucleosynthesis the computer way (1992).
- [36] R. V. Wagoner, Synthesis of the Elements Within Objects Exploding from Very High Temperatures, *Astrophys. J. Suppl. Ser.* **18**, 247 (1969).
- [37] R. V. Wagoner, Big-Bang Nucleosynthesis Revisited, *Astrophys. J.* **179**, 343 (1973).
- [38] C. Bambi, M. Giannotti, and F. L. Villante, Response of primordial abundances to a general modification of  $G_N$  and/or of the early universe expansion rate, *Phys. Rev. D* **71**, 123524 (2005), arXiv:astro-ph/0503502 [astro-ph].
- [39] K. M. Nollett and G. Steigman, BBN and the CMB constrain neutrino coupled light WIMPs, *Phys. Rev. D* **91**, 083505 (2015), arXiv:1411.6005 [astro-ph.CO].
- [40] C. Giovanetti, M. Lisanti, H. Liu, S. Mishra-Sharma, and J. T. Ruderman, LINX: A Fast, Differentiable, and Extensible Big Bang Nucleosynthesis Package, arXiv e-prints, arXiv:2408.14538 (2024), arXiv:2408.14538 [astro-ph.CO].
- [41] K. He, X. Zhang, S. Ren, and J. Sun, Deep Residual Learning for Image Recognition, in *Proceedings of the IEEE Conference on Computer Vision and Pattern Recognition (CVPR)* (2016) pp. 770–778, arXiv:1512.03385 [cs.CV].
- [42] I. Goodfellow, Y. Bengio, and A. Courville, *Deep Learning* (MIT Press, 2016) <http://www.deeplearningbook.org>.
- [43] A. Vaswani, N. Shazeer, N. Parmar, J. Uszkoreit, L. Jones, A. N. Gomez, L. Kaiser, and I. Polosukhin, Attention is all you need, in *Advances in Neural Information Processing Systems*, Vol. 30 (2017) pp. 5998–6008, arXiv:1706.03762 [cs.CL].
- [44] S. Dutta and R. J. Scherrer, Big bang nucleosynthesis with a stiff fluid, *Phys. Rev. D* **82**, 083501 (2010), arXiv:1006.4166 [astro-ph.CO].
- [45] V. A. Belinsky, L. P. Grishchuk, I. M. Khalatnikov, and Y. B. Zeldovich, Inflationary stages in cosmological models with a scalar field, *Physics Letters B* **155**, 232 (1985).
- [46] B. Spokoiny, Deflationary Universe scenario, *Physics Letters B* **315**, 40 (1993), arXiv:gr-qc/9306008 [gr-qc].
- [47] M. Joyce, Electroweak baryogenesis and the expansion rate of the Universe, *Phys. Rev. D* **55**, 1875 (1997), arXiv:hep-ph/9606223 [hep-ph].
- [48] C. Eröncel, Y. Gouttenoire, R. Sato, G. Servant, and P. Simakachorn, Universal Bound on the Duration of a Kination Era, *Phys. Rev. Lett.* **135**, 101002 (2025), arXiv:2501.17226 [hep-ph].
- [49] P. J. E. Peebles and A. Vilenkin, Quintessential inflation, *Phys. Rev. D* **59**, 063505 (1999), arXiv:astro-ph/9810509 [astro-ph].
- [50] B. Li, T. Rindler-Daller, and P. R. Shapiro, Cosmological constraints on Bose-Einstein-condensed scalar field dark matter, *Phys. Rev. D* **89**, 083536 (2014), arXiv:1310.6061 [astro-ph.CO].
- [51] Q. Yang, B. Li, and P. R. Shapiro, Hydrodynamics of ultralight complex scalar field dark matter and its impact on the growth of structure, *Science China Physics, Mechanics, and Astronomy* **68**, 280409 (2025), arXiv:2503.16773 [astro-ph.CO].
- [52] R. T. Co, L. J. Hall, and K. Harigaya, Axion Kinetic Misalignment Mechanism, *Phys. Rev. Lett.* **124**, 251802 (2020), arXiv:1910.14152 [hep-ph].
- [53] S. Weinberg, *Cosmology* (2008).
- [54] A. D. Dolgov, Neutrinos in cosmology, *Phys. Rep.* **370**, 333 (2002), arXiv:hep-ph/0202122 [hep-ph].
- [55] G. Steigman, Primordial Nucleosynthesis: Successes and Challenges, *International Journal of Modern Physics E* **15**, 1 (2006), arXiv:astro-ph/0511534 [astro-ph].
- [56] Planck Collaboration, N. Aghanim, Y. Akrami, M. Ashdown, J. Aumont, C. Baccigalupi, M. Ballardini, A. J. Banday, R. B. Barreiro, N. Bartolo, S. Basak, R. Battye, K. Benabed, J. P. Bernard, M. Bersanelli, P. Bielewicz, J. J. Bock, J. R. Bond, J. Borrill, F. R. Bouchet, F. Boulanger, M. Bucher, C. Burigana, R. C. Butler, E. Calabrese, J. F. Cardoso, J. Carron, A. Challinor, H. C. Chiang, J. Chluba, L. P. L. Colombo, C. Combet, D. Contreras, B. P. Crill, F. Cuttaia, P. de Bernardis, G. de Zotti, J. Delabrouille, J. M. Delouis, E. Di Valentino, J. M. Diego, O. Doré, M. Douspis, A. Ducout, X. Dupac, S. Dusini, G. Efstathiou, F. Elsner, T. A. Enßlin, H. K. Eriksen, Y. Fantaye, M. Farhang, J. Fergusson, R. Fernandez-Cobos, F. Finelli, F. Forastieri, M. Frailis, A. A. Fraisse, E. Franceschi, A. Frolov, S. Galeotta, S. Galli, K. Ganga, R. T. Génova-Santos, M. Gerbino, T. Ghosh, J. González-Nuevo, K. M. Górski, S. Gratton, A. Gruppuso, J. E. Gudmundsson, J. Hamann, W. Handley, F. K. Hansen, D. Herranz, S. R. Hildebrandt, E. Hivon, Z. Huang, A. H. Jaffe, W. C. Jones, A. Karakci, E. Keihänen, R. Keskitalo, K. Kiiveri, J. Kim, T. S. Kisner, L. Knox, N. Krachmalnicoff, M. Kunz, H. Kurki-Suonio, G. Lagache, J. M. Lamarre, A. Lasenby, M. Lattanzi, C. R. Lawrence,

- M. Le Jeune, P. Lemos, J. Lesgourgues, F. Levrier, A. Lewis, M. Liguori, P. B. Lilje, M. Lilley, V. Lindholm, M. López-Cañiego, P. M. Lubin, Y. Z. Ma, J. F. Macías-Pérez, G. Maggio, D. Maino, N. Mandolesi, A. Mangilli, A. Marcos-Caballero, M. Maris, P. G. Martin, M. Martinelli, E. Martínez-González, S. Matarrese, N. Mauri, J. D. McEwen, P. R. Meinhold, A. Melchiorri, A. Mennella, M. Migliaccio, M. Millea, S. Mitra, M. A. Miville-Deschênes, D. Molinari, L. Montier, G. Morgante, A. Moss, P. Natoli, H. U. Nørgaard-Nielsen, L. Pagano, D. Paoletti, B. Partridge, G. Patanchon, H. V. Peiris, F. Perrotta, V. Pettorino, F. Piacentini, L. Polastri, G. Polenta, J. L. Puget, J. P. Rachen, M. Reinecke, M. Remazeilles, A. Renzi, G. Rocha, C. Rosset, G. Roudier, J. A. Rubiño-Martín, B. Ruiz-Granados, L. Salvati, M. Sandri, M. Savelainen, D. Scott, E. P. S. Shellard, C. Sirignano, G. Sirri, L. D. Spencer, R. Sunyaev, A. S. Suur-Uski, J. A. Tauber, D. Tavagnacco, M. Tenti, L. Toffolatti, M. Tomasi, T. Trombetti, L. Valenziano, J. Valiviita, B. Van Tent, L. Vibert, P. Vielva, F. Villa, N. Vittorio, B. D. Wandelt, I. K. Wehus, M. White, S. D. M. White, A. Zaccchi, and A. Zonca, Planck 2018 results. VI. Cosmological parameters, *Astron. Astrophys.* **641**, A6 (2020), arXiv:1807.06209 [astro-ph.CO].
- [57] F. M. Gonzalez, E. M. Fries, C. Cude-Woods, T. Bailey, M. Blatnik, L. J. Broussard, N. B. Callahan, J. H. Choi, S. M. Clayton, S. A. Currie, M. Dawid, E. B. Dees, B. W. Filippone, W. Fox, P. Geltenbort, E. George, L. Hayen, K. P. Hickerson, M. A. Hoffbauer, K. Hoffman, A. T. Holley, T. M. Ito, A. Komives, C. Y. Liu, M. Makela, C. L. Morris, R. Musedinovic, C. O’Shaughnessy, R. W. Pattie, J. Ramsey, D. J. Salvat, A. Saunders, E. I. Sharapov, S. Slutsky, V. Su, X. Sun, C. Swank, Z. Tang, W. Uhrich, J. Vanderwerp, P. Walstrom, Z. Wang, W. Wei, A. R. Young, and UCN  $\tau$  Collaboration, Improved Neutron Lifetime Measurement with UCN  $\tau$ , *Phys. Rev. Lett.* **127**, 162501 (2021), arXiv:2106.10375 [nucl-ex].
- [58] G. Mangano, G. Miele, S. Pastor, T. Pinto, O. Pisanti, and P. D. Serpico, Relic neutrino decoupling including flavour oscillations, *Nuclear Physics B* **729**, 221 (2005), arXiv:hep-ph/0506164 [hep-ph].
- [59] S. Ando, R. H. Cyburt, S. W. Hong, and C. H. Hyun, Radiative neutron capture on a proton at big-bang nucleosynthesis energies, *Phys. Rev. C* **74**, 025809 (2006), arXiv:nucl-th/0511074 [nucl-th].
- [60] J. J. Bennett, G. Buldgen, P. F. de Salas, M. Drewes, S. Gariazzo, S. Pastor, and Y. Y. Y. Wong, Towards a precision calculation of the effective number of neutrinos  $N_{eff}$  in the Standard Model. Part II. Neutrino decoupling in the presence of flavour oscillations and finite-temperature QED, *J. Cosmol. Astropart. P.* **2021**, 073 (2021), arXiv:2012.02726 [hep-ph].
- [61] S. Gariazzo, P. F. de Salas, and S. Pastor, Thermalisation of sterile neutrinos in the early universe in the 3+1 scheme with full mixing matrix, *J. Cosmol. Astropart. P.* **2019**, 014 (2019), arXiv:1905.11290 [astro-ph.CO].
- [62] K. Akita and M. Yamaguchi, A precision calculation of relic neutrino decoupling, *J. Cosmol. Astropart. P.* **2020**, 012 (2020), arXiv:2005.07047 [hep-ph].
- [63] B. Li, J. Meyers, and P. R. Shapiro, Multimodality in the Search for New Physics in Pulsar Timing Data and the Case of Kination-amplified Gravitational-wave Background from Inflation, *Astrophys. J.* **985**, 117 (2025), arXiv:2503.18937 [astro-ph.CO].
- [64] B. Li and P. R. Shapiro, Precision cosmology and the stiff-amplified gravitational-wave background from inflation: NANOGrav, Advanced LIGO-Virgo and the Hubble tension, *J. Cosmol. Astropart. P.* **2021**, 024 (2021), arXiv:2107.12229 [astro-ph.CO].
- [65] B. Li, P. R. Shapiro, and T. Rindler-Daller, Bose-Einstein-condensed scalar field dark matter and the gravitational wave background from inflation: New cosmological constraints and its detectability by LIGO, *Phys. Rev. D* **96**, 063505 (2017), arXiv:1611.07961 [astro-ph.CO].
- [66] B. D. Fields, P. Molaro, and S. Sarkar, Big bang nucleosynthesis, *Reviews of Particle Physics* (2025).
- [67] D. J. Fixsen, The Temperature of the Cosmic Microwave Background, *Astrophys. J.* **707**, 916 (2009), arXiv:0911.1955 [astro-ph.CO].
- [68] B. Li, Modified PARthENoPE with a stiff component, <https://github.com/bohuarolandli/PArthENoPEstiff.git> (2025).
- [69] B. Li, Modified AlterBBN with a stiff component, <https://github.com/bohuarolandli/AlterBBNstiff.git> (2025).
- [70] In this work, we adopt  $\log_{10} \kappa_{10} \in [-7, 3]$  with a uniform prior.
- [71] M. Stein, Large sample properties of simulations using latin hypercube sampling, *Technometrics* **29**, 143 (1987).
- [72] B. Tang, Orthogonal array-based latin hypercubes, *Journal of the American Statistical Association* **88**, 1392 (1993).
- [73] D. Hendrycks and K. Gimpel, Gaussian Error Linear Units (GELUs), arXiv preprint arXiv:1606.08415 (2016).
- [74] N. Srivastava, G. Hinton, A. Krizhevsky, I. Sutskever, and R. Salakhutdinov, Dropout: A Simple Way to Prevent Neural Networks from Overfitting, *Journal of Machine Learning Research* **15**, 1929 (2014).
- [75] D. P. Kingma and J. Ba, Adam: A method for stochastic optimization, in *International Conference on Learning Representations (ICLR)* (2015).
- [76] I. Loshchilov and F. Hutter, Decoupled Weight Decay Regularization, arXiv preprint arXiv:1711.05101 (2019).
- [77] E. Auler, D. A. Berg, K. A. Olive, R. W. Pogge, J. J. Salzer, and E. D. Skillman, Improving helium abundance determinations with Leo P as a case study, *J. Cosmol. Astropart. P.* **2021**, 027 (2021), arXiv:2010.04180 [astro-ph.CO].
- [78] M. Valerdi, A. Peimbert, M. Peimbert, and A. Sixtos, Determination of the Primordial Helium Abundance Based on NGC 346, an H II Region of the Small Magellanic Cloud, *Astrophys. J.* **876**, 98 (2019), arXiv:1904.01594 [astro-ph.GA].
- [79] V. Fernández, E. Terlevich, A. I. Díaz, and R. Terlevich, A Bayesian direct method implementation to fit emission line spectra: application to the primordial He abundance determination, *Mon. Not. R. Astron. Soc.* **487**, 3221 (2019), arXiv:1905.09215 [astro-ph.GA].
- [80] T. Hsyu, R. J. Cooke, J. X. Prochaska, and M. Bolte, The PHLEK Survey: A New Determination of the Primordial Helium Abundance, *Astrophys. J.* **896**, 77 (2020), arXiv:2005.12290 [astro-ph.GA].
- [81] M. Valerdi, A. Peimbert, and M. Peimbert, Chemical abundances in seven metal-poor H II regions and a determination of the primordial helium abundance, *Mon. Not. R. Astron. Soc.* **505**, 3624 (2021), arXiv:2105.12260 [astro-ph.GA].

- [82] E. Aver, D. A. Berg, A. S. Hirschauer, K. A. Olive, R. W. Pogge, N. S. J. Rogers, J. J. Salzer, and E. D. Skillman, A comprehensive chemical abundance analysis of the extremely metal poor Leoncino Dwarf galaxy (AGC 198691), *Mon. Not. R. Astron. Soc.* **510**, 373 (2022), arXiv:2109.00178 [astro-ph.GA].
- [83] O. A. Kurichin, P. A. Kislitsyn, V. V. Klimenko, S. A. Balashev, and A. V. Ivanchik, A new determination of the primordial helium abundance using the analyses of H II region spectra from SDSS, *Mon. Not. R. Astron. Soc.* **502**, 3045 (2021), arXiv:2101.09127 [astro-ph.CO].
- [84] R. J. Cooke, M. Pettini, R. A. Jorgenson, M. T. Murphy, and C. C. Steidel, Precision Measures of the Primordial Abundance of Deuterium, *Astrophys. J.* **781**, 31 (2014), arXiv:1308.3240 [astro-ph.CO].
- [85] R. J. Cooke, M. Pettini, K. M. Nollett, and R. Jorgenson, The Primordial Deuterium Abundance of the Most Metal-poor Damped Lyman- $\alpha$  System, *Astrophys. J.* **830**, 148 (2016), arXiv:1607.03900 [astro-ph.CO].
- [86] S. Riemer-Sørensen, J. K. Webb, N. Crighton, V. Dumont, K. Ali, S. Kotuš, M. Bainbridge, M. T. Murphy, and R. Carswell, A robust deuterium abundance; re-measurement of the  $z = 3.256$  absorption system towards the quasar PKS 1937-101, *Mon. Not. R. Astron. Soc.* **447**, 2925 (2015), arXiv:1412.4043 [astro-ph.CO].
- [87] S. A. Balashev, E. O. Zavarygin, A. V. Ivanchik, K. N. Telikova, and D. A. Varshalovich, The primordial deuterium abundance: subDLA system at  $z_{abs} = 2.437$  towards the QSO J 1444+2919, *Mon. Not. R. Astron. Soc.* **458**, 2188 (2016), arXiv:1511.01797 [astro-ph.GA].
- [88] S. Riemer-Sørensen, S. Kotuš, J. K. Webb, K. Ali, V. Dumont, M. T. Murphy, and R. F. Carswell, A precise deuterium abundance: remeasurement of the  $z = 3.572$  absorption system towards the quasar PKS1937-101, *Mon. Not. R. Astron. Soc.* **468**, 3239 (2017), arXiv:1703.06656 [astro-ph.CO].
- [89] E. O. Zavarygin, J. K. Webb, S. Riemer-Sørensen, and V. Dumont, Primordial deuterium abundance at  $z_{abs} = 2:504$  towards Q1009+2956, in *Journal of Physics Conference Series*, Journal of Physics Conference Series, Vol. 1038 (IOP, 2018) p. 012012, arXiv:1801.04704 [astro-ph.CO].
- [90] H. Diao, BBNet repository, <https://github.com/Hdiao112/BBNet.git> (2025).